Title

Spatially resolved performance and degradation in a perfluorinated anion exchange membrane fuel cell

Authors

Divekar, Ashutosh G

Gerhardt, Michael R

Antunes, Christopher M

et al.

Publication Date

2022-02-01

DOI

10.1016/j.electacta.2021.139812

Peer reviewed

Spatially Resolved Performance and Degradation in a Perfluorinated Anion Exchange Membrane Fuel Cell.

Ashutosh G. Divekar,[1,2] Michael R. Gerhardt,[3] Christopher M. Antunes,[2] Luigi Osmieri,[2] Ami C. Yang-Neyerlin,[2] Adam Z. Weber,[3] Bryan S. Pivovar,[2] Guido Bender,[2,z] Andrew M. Herring,[1,z]

[1]Department of Chemical & Biological Engineering, Colorado School of Mines, Golden, CO 80401, USA.
[2]Chemistry and Nanoscience center, National Renewable Energy Laboratory, Golden, CO 80401, USA.
[3]Energy Conversion Group, Energy Technologies Area, Lawrence Berkeley National Laboratory, Berkeley CA 94720, USA.
[z] Corresponding Author E-mail Address (aherring@mines.edu, guido.bender@nrel.gov)

Abstract Text

Anion exchange membrane fuel cells may enable future operation with non-precious metal-based catalysts. These systems have a delicate sensitivity to operating conditions such as humidification levels and the presence of CO_2 in the air oxidant stream. We present spatially resolved in-situ performance results that shed light on phenomena that are unique to anion exchange membrane fuel cells. For cell construction, a highly conductive perfluorinated anion exchange polymer was used as the membrane and the material in powder form as the ionomer. Experiments were conducted to investigate the effects of humidification, fuel/oxidant concentration, and carbonation effects on the performance and its distribution in the cell. The results indicated that (i) dry conditions at the cathode have a stronger effect than at the anode on overall cell performance, (ii) performance significantly suffered when humidification was below 90%, (iii) fuel and oxidant dilution effects lead mass-transport losses and were stronger than flow rate effects, (iv) CO_2 in the cathode feed stream creates an equilibration disparity between the inlet and outlet sections and CO_2 purging is affected by flooding conditions, and (v) after >500 h of operation, performance deteriorates predominantly at the inlet.

1. Introduction

Ionic polymers used for low-temperature fuel cell applications have emerged as a promising material for energy and transportation applications over the past few decades [1, 2]. The ionic polymers are categorized as proton or anion exchange membranes (PEMs, AEMs) [3] . and PEM materials are currently used in commercially available fuel cell vehicles. The PEM fuel cell systems have to rely on expensive platinum-based catalysts, while the use of non-platinum cathode catalysts is feasible in AEM fuel cells (AEMFCs). This is due to operation at high pH which allows the OH^- to act as a charge carrier [4] . However, the AEMFC technology must overcome several challenges before it can compete with PEMFC technology, such as cell durability due to lower cationic stability and loss in performance due to carbon-dioxide reaction with the OH^- ion [5, 6] .

Automotive fuel cells require at least 5000 h of durability [4] , which is very challenging for AEMFCs. To date the highest AEM fuel cell durability was reported for a constant current density of 600 mA/cm^2 over 2000 h [7] . Two common loss mechanisms are known. On the one hand, the OH^- ion is a strong nucleophile and attacks polar functionalities in the AEM. For example, reactions such as the Hoffman elimination directly remove the polymer's functionality to conduct ions which leads to a drop in performance [3] . This can be mitigated by tethering advanced cations to the polymer which results in better alkaline stability than conventional trimethyl ammonium cations under certain circumstances [8] . On the other hand, CO_2 from the ambient air, which has a concentration of about 400 ppm, creates a major challenge for long term operation. It reacts with the OH^- anion to form HCO_3^- and CO_3^{2-} anions, a process which results in the reduction of ionic conductivity [9] . The CO_2 reaction affects the membrane properties progressively and hence the fuel cell performance is eventually lost [10].

Improved AEMs for fuel cells were first conceptualized and tested in early 2000s [4] . Until 2008, the AEM studies reported OH^- conductivity below 40 $mScm^{-1}$ at room conditions. Beyond

2008, researchers reported conductivity values <100 $mScm^{-1}$ at elevated temperatures, but after 2014, the conductivity values of 100 $mScm^{-1}$ were achieved. Very recently, some groups have even reported conductivity values close to ~200 $mScm^{-1}$ [11-13] . The significant improvements in the ionic conductivity values over the years have resulted in higher peak power performances of up to 3.4 Wcm^{-2} [*14]* . AEMs have a much wider range of chemistries than PEMs and several approaches have been shown to be successful such as synthesis and processing of block co-polymers, functionalizing perfluorinated ionomers, or optimizing radiation grafting of engineering plastics. It was realized that simply increasing IEC of the polymer does not lead to higher performance and not only leads to excessive dimensional swelling but also the cationic groups condense with each other and the conductivity plateaus [15] . Various cross-linking strategies were employed to induce a phase segregation of ionic domains in the polymer. This enabled an optimized morphology at a higher IEC and also inhibited the dimensional swelling [13, 16] . Radiation grafted polymers begin with an unfunctionalized substrate like ethylene tetrafluroethylene (ETFE) exposed to e-beam radiation to graft ionic moieties such as vinyl benzyl chloride (VBC) onto the polymer in a controlled manner [17] , which has been optimized [18-21] .

The fabrication of MEAs with existing and novel AEM materials requires the successful integration of ionomers that are compatible with conventional ink-based electrodes [22]. Recently, Mustain and co-workers have demonstrated that using the ground powder form of an AEM material in the electrode can produce high performing membrane electrode assemblies (MEAs) [7] . With the availability of high performing MEAs practical aspects of fuel cell operation can move into the focus to improve AEMFC performance and lifetime. It is for example informative to understand the spatial performance of the cell. Such studies can shed light on effects of water

management, ionomer carbonation, hydrogen and oxygen concentration, and degradation mechanisms.

Researchers have used segmented fuel cells (SFC) since decades to study the spatial performance in PEMFCs. The diagnostic tool was introduced by Cleghorn et al. and Stumper et al., and further refined and customized over the years to address specific research questions [23-27]. Researchers have gained valuable insights using SFC systems to understand the effect of humidification, electro-osmosis, back-diffusion, temperature, inlet pressure, clamping pressure, flow rate, flow-field design, flow configuration, and contaminant species on the spatial PEMFC performance [28].

For the benefit of the reader a short review of the SFC research on PEMFC is given in the following paragraphs. Most of the SFC are capable to quantify the current distribution of the cell at various humidification levels. In PEMFC, at a lower inlet humidification, the cell is required to intrinsically hydrate using product water which leads to a performance gradient from this operating condition [29-32]. At a sufficiently high humidification the distribution becomes more uniform but may also lead to a higher presence of liquid water in the cell which may result in flooding and mass-transfer limitations near the end of the flow channel [25, 31, 33] . Increases in the gas flow resistance due to flooding results in the reduction of cell performance downstream and also develops shortcut gas flows [34]. Strong performance gradients may further lead to local temperature increases [35] . In PEMFCs, the SFC has been used to study the transition of water management dominance from electro-osmotic drag of water (anode to the cathode due to the transport of protons) to the back-diffusion of water (cathode to the anode driven by a concentration gradient) [36]. Dong et al. have reported that a higher humidification leads to improved cell performance and that sufficient anode humidification avoids local dry out and performance losses

[37] . In contrast to PEMFC systems, the direction of electro-osmotic drag and back-diffusion is reversed in AEMFC: electro-osmotic drag occurs from the cathode to the anode with the transport of hydroxide ions and the back-diffusion of water from the anode to the cathode, driven by the resulting water gradient. Results of the spatial effects of these water management governing processes on the AEMFC system are presented in the results and discussion section of this work.

Flow-rates and gas composition effects have also been studied on PEMFC systems. The current density distribution in the SFC is more dependent on the oxygen utilization rather than the fuel and is non-uniform at low airflows due to the O_2 starvation effect [31, 38, 39] . On the one hand, at low air flows, the current density declines in the downstream segments due to oxidant depletion and flooding of liquid water generated upstream in the channels [40-43]. On the other hand, higher airflow rates improve liquid water drainage and reduce MEA flooding [44], but may also dry out the oxidant inlet [45]. Factors such as low pressure conditions, gasket material, clamping pressure affecting the flooding and gas flow resistance are studied using SFC [34, 44] .

SFC systems can further assist in understanding and optimizing effects of the cell architecture such as the type of flow field [46]. Another critical loss mechanism is the introduction of contaminant species into the feed stream of the cell. For example, in AEMFCs the CO_2 that is present in air significantly reduces the performance by impacting the conductivity of the alkaline electrolyte membrane. This process is expected to show a time and spatial dependency along the flow-field, similar to most of the reported PEMFC contamination processes. One critical contaminant for mobile PEMFC applications is CO, which was extensively studied using SFC systems [47-49].

All this work indicates how useful the SFC diagnostic tool is for understanding the processes within a fuel cell that cannot be observed through single cell experiments. In this work the SFC

diagnostic is applied to an AEMFC system. The work employs a previously introduced novel perfluorinated anionic membrane [50, 51]. The AEM is synthesized from a perfluorinated sulfonyl fluoride ionomer precursor (EW 798) developed by 3M (USA). It is a copolymer of tetrafluoroethylene (PTFE) and a trifluoroethylene functionalized with a perfluorinated sulfonyl fluoride carbon chain. The trimethylammonium cation is tethered to the sulfonamide through a six-carbon alkyl spacer chain [51]. We present spatial experimental results that demonstrate the performance effects of hydration, fuel or oxidant starvation, CO_2 poisoning, and degradation. For analysis, we compare the results to a modelling study that highlights the physics of the occurring processes.

The employed SFC features 121 segments within a 50 cm^2 active area [52], and is used to study the dependence of the spatial current distribution in an AEMFC on various operating conditions and the flow-field architecture. For PEMFCs, water is generated at the cathode whereas for the AEMFCs it is a reactant at the cathode as well as a product at the anode. Therefore water management is complicated and needs to be understood thoroughly for optimal performance [53].

In summary, most of the studies on AEM that are available in the literature are focused on developing new membrane material, developing catalyst inks for higher performance and understanding the carbonation phenomenon [4, 53, 54]. This work employs for the first time a SFC diagnostic to study fundamental processes associated with AEMFCs with the intention to increase understanding of the effect of various operating conditions on the spatial current distribution and shed more light on MEA durability in AEMFC.

2. Experimental

2.1 AEM Materials:

Perfluorinated anion exchange membrane was prepared in two thicknesses of 70 and 35 μm,

using PFAEM_CH3_C6 polymer synthesized from perfluorinated sulfonyl fluoride ionomer precursor (EW 798, 3M USA) as described previously [50, 51]. Powder of the same material were used as ionomer in the electrode.

2.2 MEA fabrication:

To create an electrode ink, the polymer from the previous section was ground to a fine powder in a mortar and pestle and mixed with 46% Pt on Vulcan® carbon (Alfa Aesar HiSPEC 4000) catalyst. A small amount of DI water (3 ml) was added to the catalyst mixture and ground for an additional 10 min to avoid aggregation of the particles. The slurry was transferred to a vial and 2-propanol was added (to a total of 27 cm^3) to the mortar to rinse the residue. The addition of 2-propanol to the mortar was repeated 2–3 times to ensure that almost all of the ink slurry was collected. The final ink was tip sonicated for 10 seconds and then bath sonicated in an ice bath for 20 min before it was hand-sprayed onto a 50 cm^2 GDL (Toray® TGP-H-060) which contained a 5% PTFE wet proofing. The Pt loading of these electrodes was 0.30-0.40 mg/cm^2. For select straight channel flow-field experiments the 50 cm^2 GDL was cut into 0.64 cm x 7.2 cm strips. The resulting electrodes were one segment row wide and slightly larger than the single-channel length. The Pt loading of these electrodes was 0.45-0.60 mg/cm^2.

2.3 Segmented Fuel Cell:

NREL's SFC consists of a cell hardware with a segmented cathode flow-field connected to a printed circuit board (PCB) current collector plate as shown in the schematic in figure 1**Error! Reference source not found.**. The PCB is further connected to a multi-channel electronic load system for application of current. This system is connected to a spatial data acquisition system (3M/Caltronics). And, fuel cell test station (Fuel Cell Technologies) is used for operating the cell hardware. The spatial data is visually and numerically presented by using in-house developed

software. The net active area of the cell is 50 cm^2, which is divided into 121 segments (0.413 cm^2 each) in a 11x11 matrix. Visual representation of the hardware is presented by Osmieri et al. [55].

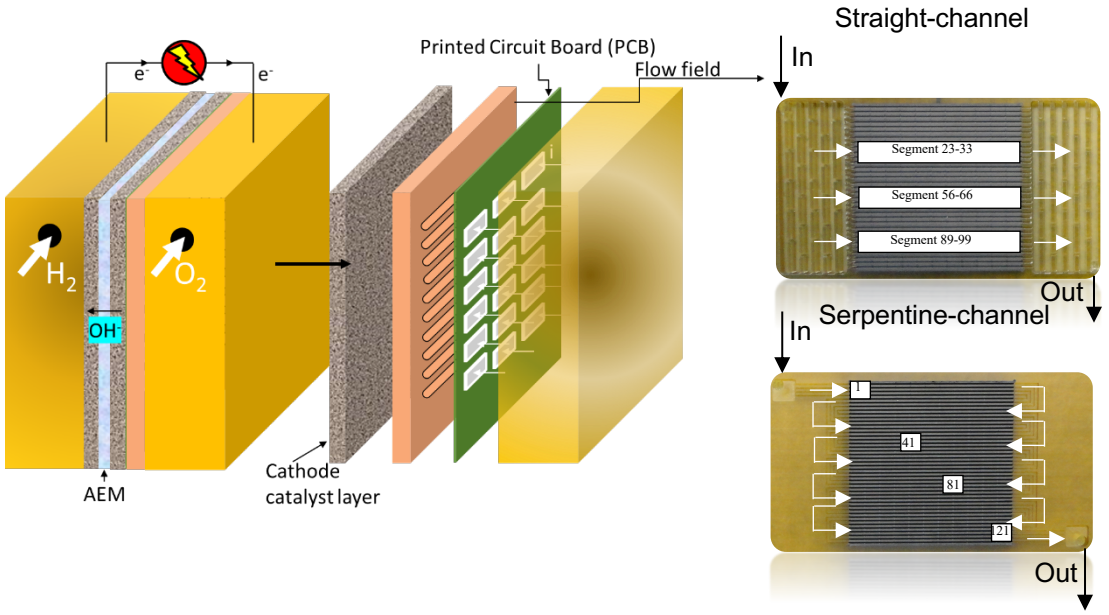

Figure 1: Schematic representation of segmented fuel cell hardware.

The hardware supports 4-wire voltage sensing at each segment with identical current carrying trace lengths for all segments which enables homogeneous current distribution by design. Two different flow-fields were used in this study: (i) a straight channel flow-field with three flow channels per each segment width, and (ii) a 4-channel serpentine flow-field with 11 rows and bends outside of the active area. All channels were 1 mm wide and 0.83 mm deep. The cathode flow field consists of graphite flow channels and graphite segment squares on the back side separated by insulation for current conduction through the printed circuit board. Whereas, the anode flow-field is un-segmented and serpentine. The fuel cells are operated in a co-flow. The typical experiment of this study employed the straight channel flow-field. For this setup, three electrode strips were carefully aligned with three rows of the hardware. Adjacent flow channels and all other flow channels that were not used were blocked with regards to gas flow and gasketed off with PTFE

gaskets. Additional experiments were performed on the entire 50 cm^2 active area using the serpentine flow-field.

2.4 MEA conditioning, assembly, and testing procedure:

Prior to assembly the membrane and gas diffusion electrodes (GDEs) were ion exchanged in 1M KOH over a period of 24 h at room temperature. The solution was exchanged 3 times in regular intervals. Subsequently, the materials were thoroughly rinsed with DI water. For cell construction, the membrane was assembled between two GDEs and secured in the SFC hardware. PTFE gaskets of a specific thickness were selected to reach a GDE compression of 20% when tightening the cell with a torque of 50-inch lbs. The temperature of the cell was kept at 60°C.

Diagnostics:

X-ray fluorescence spectroscopy (Fischer FISCHERSCOPE® X-RAY XDV®-SDD) was used to determine the Pt/C loading of the electrodes. WinFTM EDXRF software (version 6.35-S-PDM) was used to map the catalyst loading at all segment positions. Infrared spectroscopy of pre-tested and post-tested membrane segments was performed to observe chemical changes within the polymer over the course of the experiments using a Nicolet™ iN™10 Infrared Microscope. Samples were vacuum dried overnight before any IR characterization.

2.5 Theoretical fuel cell model:

The experimental studies were complimented by modeling studies to increase understanding of the investigated processes. The model used is a macrohomogeneous mathematical model combining a 2D cell model with a 1D down-the-channel model. This approach allows for modeling of down-channel and land-channel effects while avoiding the computational cost and complexity of a 3D model. This model, which employs an AEM sandwiched between two catalyst layers and gas diffusion layers has been previously published and validated for AEM fuel cells [56].

The model contains Darcy two-phase flow within the porous-transport, gas-diffusion, and catalyst layers, Stefan-Maxwell-Stefan multicomponent diffusion in the gas phase and coupled water-anion transport in the membrane and ionomer phase. Water is modeled as existing in three distinct phases: the gas and liquid phases within the CL and GDL, as well as an ionomer-bound phase existing within the CL and membrane. Gas-phase water transport occurs via convection (Darcy's law) and diffusion (Stefan-Maxwell), liquid-phase water transport occurs via convection, and ionomer-bound water transport occurs via diffusion down its chemical potential gradient coupled with an electroosmotic drag flux due to the motion of hydroxide as described in previous work [56-58]. The various transport equations are coupled by source terms describing reaction kinetics and water phase changes, and an overall energy balance computes the temperature profile through the cell. For a complete listing of the model equations and properties used, see Tables S1-S16 and Figure S1 in the Supplementary Information.

The following boundary conditions were used. The temperature was set to 60°C at the GDL/land and GDL/channel boundaries for the anode and cathode, respectively. At the GDL/channel boundaries, the initial gas compositions were set to 100% H_2 at the anode and air (21% O_2, 79% N_2) at the cathode. Relative humidity is specified in each figure and initial anode/cathode gas pressures of 130/130 kPa were used. No-flux boundary conditions are used at each CL/membrane interface for liquid and gas transport and electronic current. No-flux boundary conditions are also used at each CL/GDL interface for ionic current, and water bound to the membrane. The potential was set to the applied cell potential (0.5 V) at the cathode GDL/land boundary and to 0 V at the anode GDL/channel boundary. At each channel/GDL interface, a liquid flux boundary condition is set, as described in earlier work [56, 59], which amounts to no liquid flux allowed unless the liquid pressure rises above a threshold value based on the gas pressure.

The dry gas inlet flow rates were chosen to match the stoichiometric flow rates of the relevant experiments: 2600 sccm (air) or 1000 (O_2) on the cathode and 700 sccm (H_2) on the anode, unless otherwise noted.

The gas pressure at the GDL/channel boundary in each segment is adjusted as described in Table S15 (Supplemental Information) to account for pressure drop along the channel due to Poiseuille flow. Additionally, to account for enhanced mass transport at the regions near the bends in the serpentine flow field, a sinusoidally-varying term was added to the gas pressure to artificially raise the gas pressure near the bends and lower the gas pressure in the middle of the channel. This procedure approximates the changes in mass transport due to enhanced convection within the GDL, but neglects pressure changes associated with the curved flow path.

The model comprised separate domains for each gas diffusion layer, each catalyst layer, and the membrane. The mesh comprised 10,000 rectangular domain elements and 700 boundary elements. The mesh density was increased within the CLs and membrane, and further increased at each CL/membrane interface. The model was solved using COMSOL Multiphysics® version 5.4. The channel stepping algorithm was implemented in MATLAB version R2013a. A MATLAB script executed the COMSOL model for the first channel segment, recorded the solution, updated the boundary conditions, and recomputed for the following segment, repeating until 121 channel segments had been computed.

3. Results and Discussion

Generally, this study can be separated into two high-level categories that investigate (i) the effects of key operating parameters and (ii) the chemical phenomena leading to loss in conductivity and thus performance. The key operating parameters all have their own subsection addressing inlet gas humidification levels, flow rate, and concentration. The two chemical phenomena, i.e.,

hydroxide attack and carbonation are also described in their own subsections. Note that the typical performance measured in a standard 5 cm^2 cell is higher than the performance presented here. This performance can reach as much as ~1.75 A/cm^2 at 0.5 V (~1 W cm^{-2} peak power density) for H_2/O_2 at 60°C and 85/85% RH [10]. The lower performance obtained for this particular work was associated with higher ohmic contact resistances that originated from the hardware assembly. It's also possible that the ionomer to catalyst ratio as well as coating methodology needs to be optimized to get best porosity and electrochemical active area for the larger cell. Also, Mustain and co-workers have recently published that the dew points need to be optimized at each current density condition and operating the cell at fixed dew-points could be detrimental for the cell [60]. The discussion of the results therefore focuses on the qualitative trends of the experimental results which hold true, and not on the absolute experimental values. The spatial learnings from the lower performing MEAs are also applicable to an Anion exchange CO_2 separation unit which will be discussed in detail in the carbonation section.

3.1 Hydration effects on spatial current in a serpentine channel

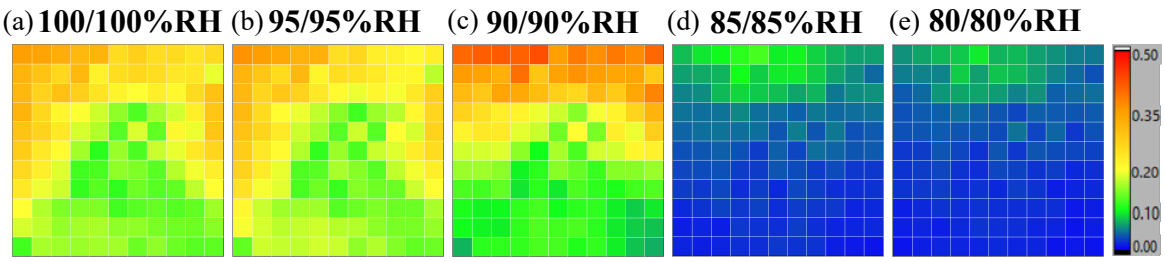

Figure 2: Current density maps of serpentine flow-field data collected at (a)100/100, (b) 95/95, (c) 90/90, (d) 85/85, (e) 80/80%RH for anode/cathode compartment respectively. The cell temperature is 60 °C and operated in current control mode of 10A[stoichiometry-10(H_2), 15(Air)] for 100, 95, and 90%RH; 2A [stoichiometry-50(H_2), 75(Air)] for 85%RH, and 1.5A for 80%RH Note: The values of cell performance are in current density (A/cm^2). Inlet of the serpentine flow channel is on top left and outlet is on the bottom right. The flow rates of H_2 and Air are 700 sccm and 2600

sccm respectively. The air used in this experiment has <3 ppm CO_2.

Figure 2 shows the current distribution of the cell for various humidification conditions ranging from 100/100 to 80/80% relative humidity (RH) at the anode/cathode, respectively. Figure 3A shows the same performance data plotting the individual segment performance along the segment position of the flow field and the its respective baseline polarization curves are shown in figure S2A.

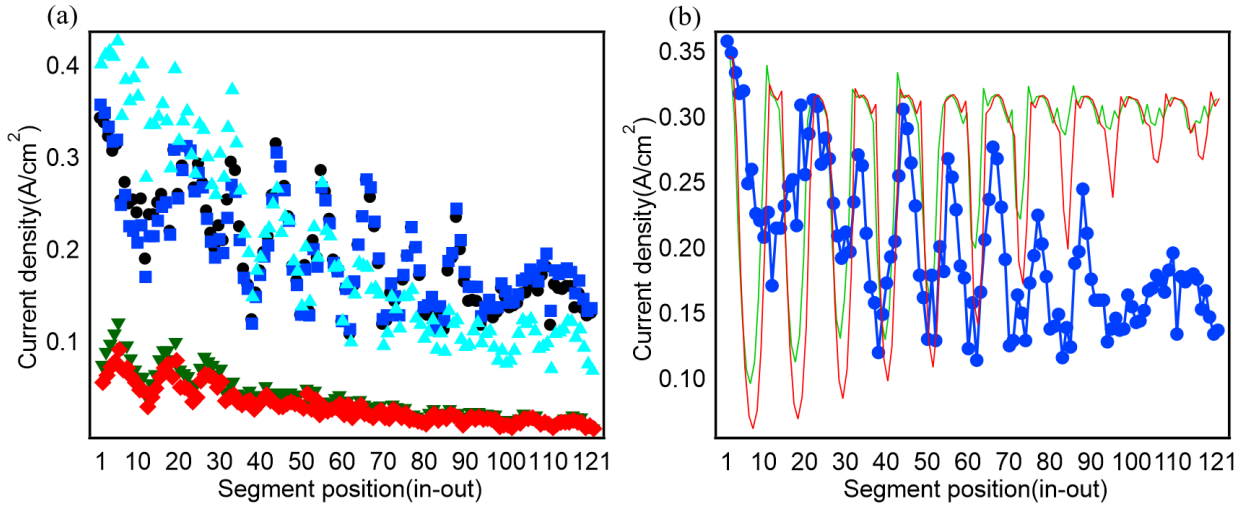

Figure 3: Current density for a serpentine flow-field segmented cell (a) Current density vs segment position of the above data where: Black circles-100% RH, Dark blue squares- 95% RH, Light blue triangles- 90% RH, Green inverted triangles- 85% RH, Red diamonds- 80% RH. The voltage at each condition was in the range of 0.35 - 0.55V. (b) Comparison of segmented cell experimental performance (95%RH-blue circles) with modelling predicted performance across the serpentine flow-field due to sinusoidal pressure variation of 90-130 kPa (green), 80-130 kPa (red).

The data in Figure 2 and 3A indicate a fluctuating performance decrease trend along the flow channel from the inlet segments toward the outlet segments for all humidification conditions. This decrease is due to accumulation of water in the downstream segments due to water generation upstream from the fuel cell reaction which acts as a mass-transport barrier for the gases to reach

the active sites. Overlaid onto this decrease are regular fluctuations of local performance. These are observed at the segments that are positioned at the edge of the flow field. A similar fluctuation of the edge segment performance has been reported in previous PEMFC work that utilized either the same [52] , or different SFC architectures [46]. The local performance increase at the edges and relatively lower at the center may be attributed to an increased pressure drop at the bends leading to an enhancement of the mass transport at this location. Figure 3B shows that the 1+2D computational model could confirm this pressure effect. By varying the gas pressure as a proxy for enhanced mass transport within a segment, the model qualitatively reproduces the observed fluctuations.

As indicated by the data in Figure 2 and 3A, on the one hand, the inlet current density is the highest when the cell is operated at 90/90% RH which is attributed to effective evaporative convection in the inlet section [60]. However, the polarization curves in Figure S2A suggest that the performance is very identical for cell operated above 90/90% RH. The performance is inferior at lower current densities but shows higher limiting current density at 90/90% RH. The loss in performance at low current density is attributed to higher susceptibility of flooding downstream due to increased cell performance near the inlet which is shown in figure 3A and increased cell performance at high current density is due to appropriate balance of water consumed and reacted at the cathode and anode respectively. On the other hand, there is a significant drop in cell performance below 90/90% RH. Several causes may contribute to this performance drop: (a) water molecules become unavailable for the production of OH^- ions at the cathode compartment [(*60*), (b) the water back-diffusion from the anode compartment is not effective enough to mitigate the net deficit of water at the cathode, and (c) the cathode is drying out leading to a loss in local ionic conductivity. The inherent hydroxide conductivity of the membrane at 95% RH is almost twice of

85% RH, which was determined in separate ex-situ conductivity experiment shown in Fig. S3A. Although the membrane still has some OH^- conductivity at 85%RH, we see that the performance getting severely deteriorated (figure 2D-E & S2A) which is hypothesize to be due primarily to cathode dry out (discussed in 3.2). The dry out is due to consumption of H_2O molecules, which directly affects the ionomer-to-ionomer particle network in the cathode layer. This network connectivity is a strong function of hydration and thus external humidification of the inlet gas. The operating window of humidification for the powder ground electrodes is very narrow which has also been previously reported by Mustain and co-workers [62]. They have also shown that the cause of this narrow window of operation is the excessive swelling of the ionomer in the anode catalyst layer which was confirmed by in-operando study [60].

3.2 Hydration effects on spatial current in a straight channel cell:

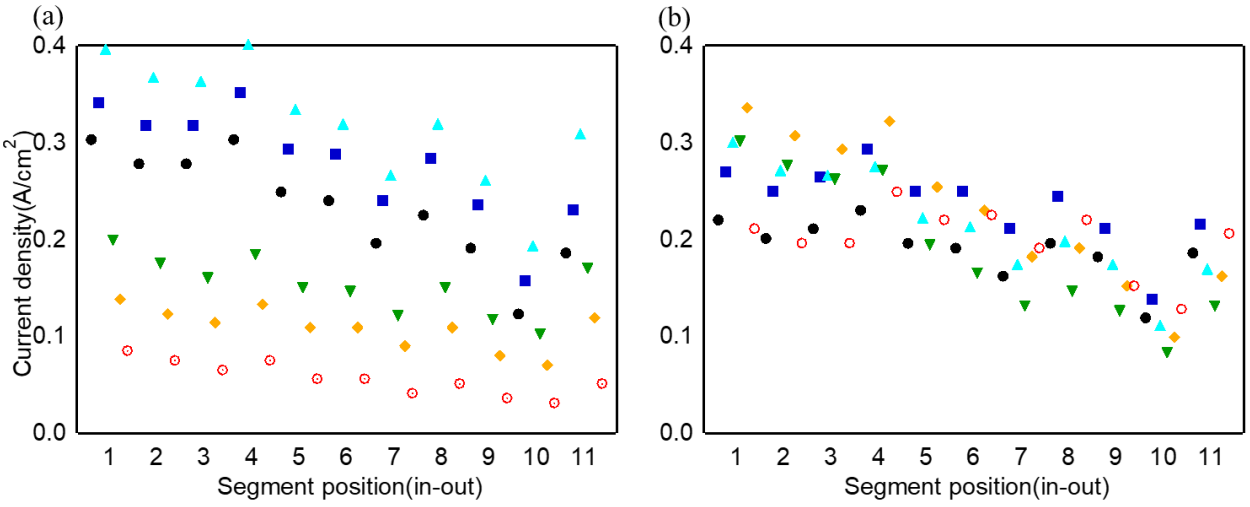

Figure 4: Current density at 0.5V for a straight-line flow-field segmented cell (a) Hydration variation on the cathode from 75% to 100%RH with, 100% RH at the anode. (b) Hydration variation on the anode from 75% to 100%RH with, 100%RH at the cathode. The fuel cell was operated at 60 °C with H_2/Air (<3 ppm CO_2) Where: Black circles-100%, Dark blue squares- 95%, Light blue triangles- 90%, Green inverted triangles- 85%, Orange diamonds- 80%, Red open

circles- 75%RH). Note: The flow rates of H_2 and Air are 1000 sccm and 2500 sccm respectively.

The data discussed in Figure 2 and 3 indicate that the bends of the serpentine flow-field impact the localized pressure at the segment, leading to performance fluctuations. Figure 4 shows representative data collected on a single segment strip using the straight channel flow-field design. The lack of bends in this architecture avoids pressure variation and disturbances of the gas flow and the length of the gas channel is reduced to the geometric width of the active area. Figure 4A shows the effect of varying the relative cathode humidity from 75% - 100% RH while keeping the anode humidity at 100%RH. The performance of the cell decreases downstream after segment 4 at all humidity conditions; however, the performance decline is more severe at higher humidification. This is attributed to the accumulation of generated water downstream leading to mass transfer losses from flooding [33]. In an AEMFC, water management is crucial because in contrast to PEMFCs water is produced at the anode and consumed at the cathode [61, 62, 63]. In addition water is further depleted at the cathode due to electro-osmotic drag with the transport of hydroxyl ions through the membrane. Similar to the PEMFC performance losses that have been reported due to anode dry out [37], our data indicates that AEMFC performance can be impacted significantly by cathode humidification. For our cell, a 90% RH cathode feed stream resulted in optimum performance, in agreement with the results from Omasta et al [62] . The water balance within the cell is complicated with factors including water consumption at the cathode, water production at the anode competing with water flux across the membrane based on current density and associated electro-osmotic drag versus back-diffusion. This water balance is not only an issue for hydration within the membrane electrode assembly but can lead to flooding in the electrodes and/or gas diffusion layers.

Figure 4B shows a similar data set for varying the anode humidity while keeping the cathode

humidity constant. The results indicate that the cell is much less sensitive to the anode humidification. The variation of the cell performance with anode humidity is relatively small, specifically in a range of 80-90% RH. It appears that flooding reduces the performance above 90% anode humidification. At humidification below 80% RH a general loss of membrane conductivity may be responsible for the net performance loss. Once more the spatial variation of the performance begins downstream of segment 4.

In summary, a fine line between dry-out at the cathode and flooding at the anode exists that needs to be met for optimizing cell performance. Uniform and maximum performance was only observed for the first four segments, indicating that local operating conditions rapidly change along the flow-field, i.e., in our case over a length of 2 cm. This strong spatial dependence may need to be mitigated for successful optimization of performance and development of industrial cell sizes.

3.3 Effect of flow rate on cell performance:

Figure 5A shows the dependence of cell performance due to variation of the anode flow rate from 50 (stoichiometry~2.23 at 0.23 A/cm^2) to 700 sccm (stoichiometry~27 at 0.28 A/cm^2) at a fixed very high cathode flow rate of 2500 sccm CO_2 free compressed air in an attempt to focus on anode effects by achieving nearly unchanging conditions within the cathode flow channel. Figure 5B shows similarly the cell performance dependence on the cathode flow which was varied over a range of 100 to 1500 sccm at a fixed very high anode flow of 1000 sccm. In both cases the cell was operated at 60°C and 95/95% RH. The sensitivity of cell performance with regards to anode flow rate was relatively minor for a stoichiometry range of 2.23 to 27. For example, when varying the anode flow rate, the segments show an increased performance at the maximum anode flow rate, particularly developed at the first four segments (~50 mA/cm^2). At all other anode flow rates, the performance was similar throughout the cell. The data indicate that the sensitivity to the

anode stoichiometry is smaller than to other processes that govern performance such as the water management. When the cathode flow rate was varied, a small decrease in performance was observed when reducing the flow rate. For the conditions tested, the data indicate that the cell performance is more dependent on the cathode flow rate than the anode flow rate. When reducing the cathode flow from 2500 sccm, i.e., the fixed flow of Figure 5A, the overall performance of the cell dropped for example from maximum performances of >0.3A/cm^2 to performance <0.2A/cm^2. The current distribution of the cell changed as well, showing a much stronger decline from inlet to outlet along the flow-field.

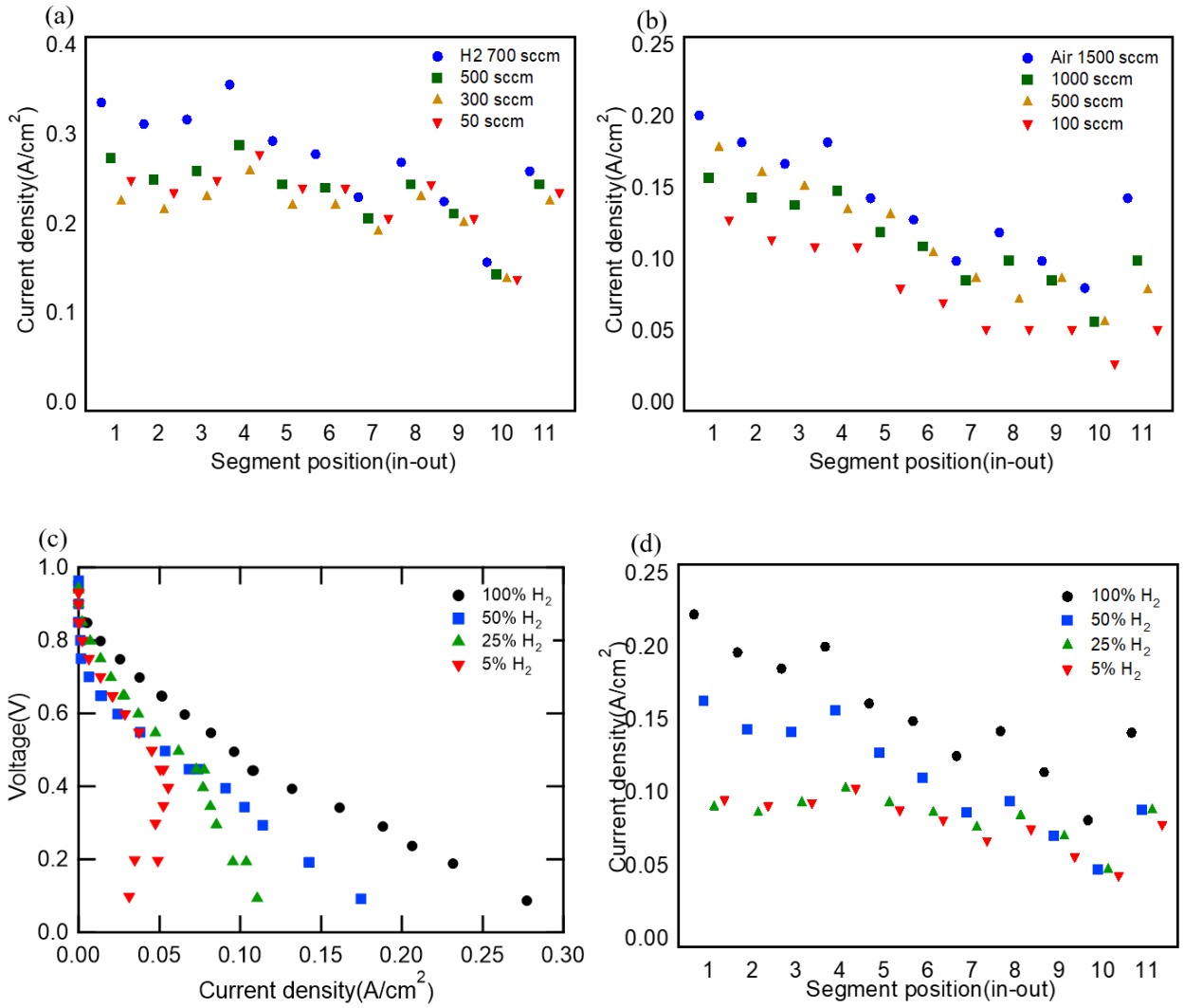

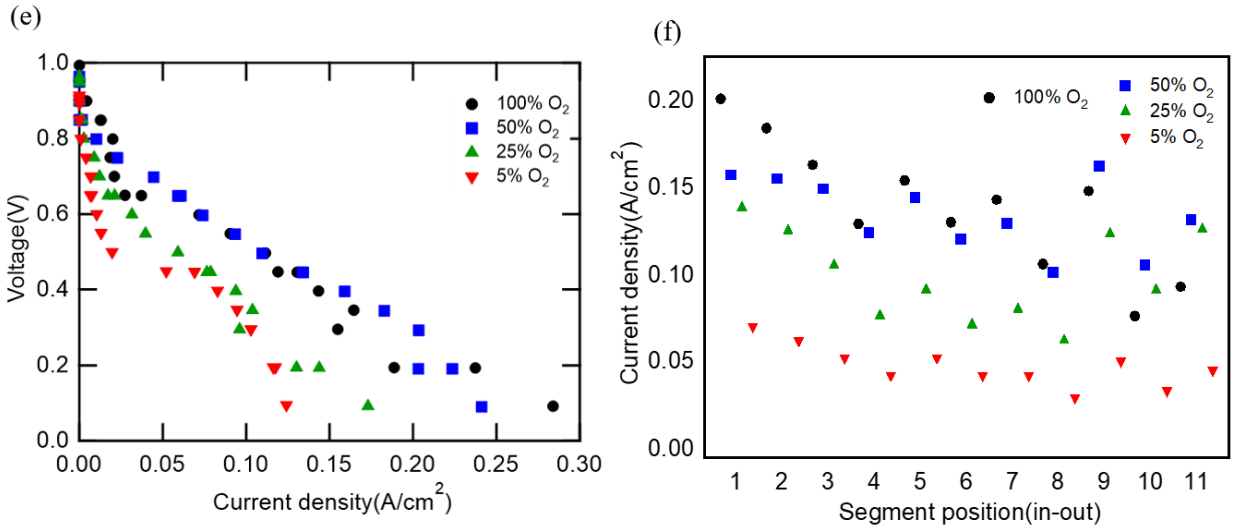

Figure 5: (a) Flow rate variation on anode from 700 to 50 sccm with flow rate, 2500 sccm at the cathode. (b) Flow rate variation on cathode from 1500 to 100 sccm with flow rate, 1000 sccm at the anode. Fuel cell operated at 60 °C, H_2/Air (< 3 ppm CO_2), 95/95%RH at anode/cathode, constant voltage 0.5V. Note: Fig (a) Blue circles-700, Green squares- 500, Orange triangles- 300, and red inverted triangles- 50 sccm. Fig (b) Blue circles- 1500, Green squares- 1000, Orange triangles- 500, and red inverted triangles- 100 sccm. (c) Polarization curve of the overall cell voltage vs current density(A/cm^2) at 100, 50, 25 and 5% H_2 diluted with N_2 (anode) and 100% O_2 (cathode). (d) Current distribution of cell performance at a constant voltage of 0.5V along the segments from inlet to outlet at 100 (stoichiometry 33 at 0.156 A/cm^2), 50 (stoichiometry 24 at 0.11 A/cm^2), 25 (stoichiometry 16 at 0.08 A/cm^2) and 5 % (stoichiometry 3.3 at 0.08 A/cm^2) H_2 diluted with N_2. (e) Polarization curve of the overall cell voltage vs current density(A/cm^2) at 100% H_2 (anode) and 100, 75, 50, 25 and 5% O_2 diluted with N_2 (cathode). (f) Current distribution of cell performance at a constant voltage of 0.5V along the segments from inlet to outlet at 100 (stoichiometry 38 at 0.14 A/cm^2), 75 (stoichiometry 36 at 0.11 A/cm^2), 50 (stoichiometry 20 at 0.13 A/cm^2), 25 (stoichiometry 13 at 0.1 A/cm^2) and 5 % (stoichiometry 5.5 at 0.05 A/cm^2) O_2 diluted with N_2. Note: Net inlet flow was kept constant at 1000 sccm for all fuel as well as oxidant

dilutions and the cell was operated at 60 °C with 95/95%RH in anode or cathode compartment.

In summary, the data suggest that the cell performance of the operated strip cell is not very sensitive to the range of flow rates that were applied. Generally, the cell performance was more affected by the cathode flow rate than the anode flow rate. However, when using very high cathode flow rates, the performance significantly improved indicating that mass transport loss may dictate the performance of the cell [44].

3.4 Hydrogen and Oxygen concentration effects:

Figure 5C and E show polarization curves of the segmented strip cell operated with a range of hydrogen or oxygen concentrations, respectively. Experiments were performed by diluting either the H_2 or the O_2 feed stream with N_2, operating otherwise at 60°C, 95/95% RH, ambient/ambient pressures, and 1000/1000 sccm flows for anode/cathode, respectively. The data in Figure 5C indicate that by reducing the concentration of the hydrogen in the feed gas the performance of the cell is lowered. Generally, the performance drops by similar amounts for all diluted feed streams for current densities lower than 0.05 A/cm^2. Above that threshold limiting currents become apparent first for 5% at 0.05 A/cm^2, then for 25% H_2 mixtures at about 0.1 A/cm^2. Note that the stoichiometry, even at the highest dilution, was never reduced to below 1.5, which indicates that significant mass transport may occur to the active sites in the electrode. This process may be influenced by the architecture and morphology of the electrode, which in our case contained a ground polymer powder as ionomer. The data in Figure 5E shows a similar data set for lowering the oxygen concentration at the cathode. Above 25% O_2, the performance impact is negligible. Below 25% O_2 however, a performance impact becomes noticeable through an initial sharp decline of the current in the kinetic region followed by some recovery at current densities above 0.05 A/cm^2. The limiting current density for 25% (stoichiometry 8 at 0.17 A/cm^2) and 5%

(stoichiometry 2.1 at 0.2 A/cm^2) O_2 in the feed stream is larger than 0.1 A/cm^2 and thus higher than that of the same H_2 concentrations (stoichiometry 14 at 0.09 A/cm^2 and 2.7 at 0.098 A/cm^2 each, Figure 5C). Although, stoichiometry value is similar to that of O_2 in 5% case, the minimal effect on limiting current density is because each water produced needs twice moles of hydrogen compared to oxygen. The overall fuel cell performance was found to be more sensitive to the H_2 dilution as compared to O_2 dilution due to over-potential losses on dilution and higher moles of H_2 consumed in the reaction.

Figure 5D and F show the current distribution of the same measurements at a cell voltage of 0.5 V. The data in Figure 5D at H_2 concentrations above 25%, the cell performance of the four inlet segments is the highest, followed by a steady performance decline along the flow-field from inlet to outlet segments. At and below 25% H_2 concentration the difference between the first four segments and the remainder of the cell becomes less distinct and a nearly uniform current distribution is observed with a slight drop near the outlet segments. Figure 5F shows the current distribution at different oxygen concentration. The performance decreases for all segments when decreasing the oxygen concentration of the feed stream, however, the general performance trends remain identical. For all oxygen concentrations, the performance decreases for the first four segments, then becomes constant for segments 5-8, before it increases slightly towards the outlet again.

3.5 Spatial performance due to cell degradation:

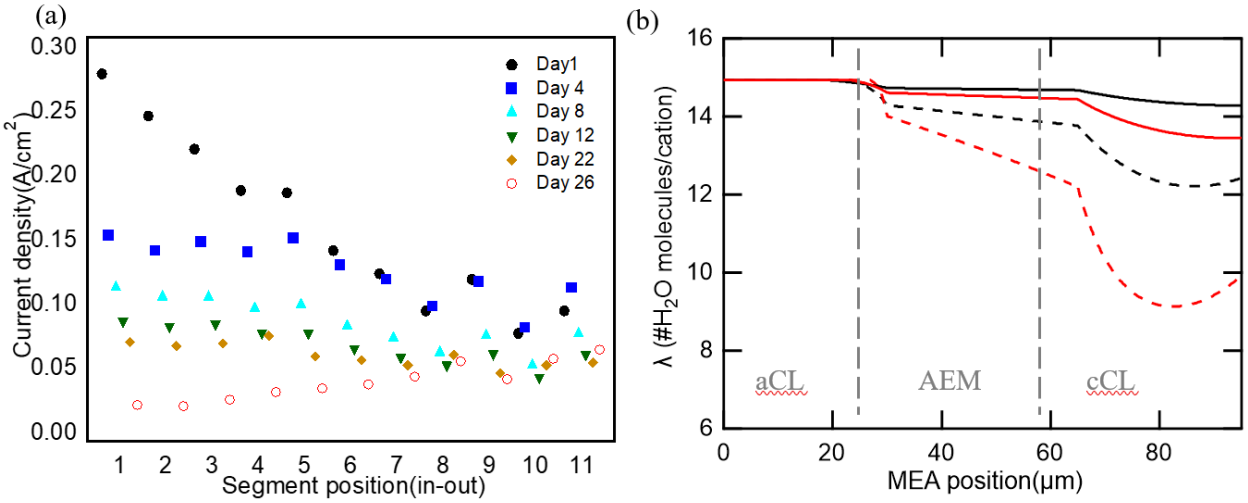

Figure 6: (a) Current distribution at a constant voltage of 0.5 V collected over a period of 26 days for a cell operated at 60 °C, 100/100 %RH at anode/cathode using pure H_2/O_2. (b) Water content per cation across the MEA at segments 1 (red) and 11 (black). Solid lines use water transport coefficient values as reported previously [56], and Table S13; dashed lines reduce the liquid- and vapor-equilibrated water transport coefficients by a factor of 10 relative to the values reported previously [56], and Table S13. Note: The flow rates of H_2 and O_2 are 1000 sccm respectively.

Figure 6A shows the progression of the spatial current density distribution of the cell over a period of 26 days of operation. While the performance of the upstream segments significantly decreases, performance of the downstream segments remains much more constant. For example, the performance of segment 1 decreases from 0.275 A/cm^2 to 0.025 A/cm^2 over the course of the 26 days, whereas that of segment 11 decreases only from 0.094 A/cm^2 to 0.064 A/cm^2. The performance change is so dramatic, that the downward performance trend along the flow-field transforms into an upward trend after 22 days of cell operation.

The observed changes may be attributed to either changes in the membrane chemical properties or in the electrode itself. Due to limitations on electrode diagnostics, we have studied only the membrane in this particular study and we plan to do more work on electrode diagnostics

in the future. However, it must be noted that Lafforgue et al. provides physical and chemical evidence that Pt-based nanocatalysts catalyze the electrochemical corrosion of the carbon support [64]. They have reported that this caused by oxidation of oxygen-containing surface groups of the carbon support upon adsorption of hydroxyl groups on the Pt-based surface. A significantly stronger degradation of the membrane is observed at the inlet section than at the outlet section. The inlet section has the highest performance at the beginning of life, which means it also has the highest current which equates to the highest water consumption and production rates on the cathode and anode, respectively. The local water balance would be expected to impact the degradation. The higher current density in the inlet section would result in more water consumption/production and increased probability of flooded or dehydrated conditions. This observation is supported by our modeling results. Figure 6B shows calculations of the water content per cation across the MEA. Solid lines employ values for operation at a higher current density, while dashed lines represent values for a lower current density for both the inlet (red) and the outlet (black) segments. The calculation results show that the higher current density in the inlet section results in lower water content at the cathode than in the outlet section. This effect can be further accelerated when the water transport within the membrane decreases due to degradation that occurs over prolonged operation. This dry out effect can promote OH^- ion attack on cationic head groups primarily in the ionomer of the cathode and may thus be contributing to the observed degradation at the inlet [65].

After 26 days of operation the chemical bond identities of the membrane was characterized with FTIR. Studying FTIR on the electrode was very difficult due to limited contrast between the polymer chemical bonds and catalyst resulting from intense Pt & C features, however, it is possible to study the membrane pre and post operation. Hence, we show the results for the inlet and outlet

sections of the membrane in the device as well as a pristine membrane sample in Figure 7.

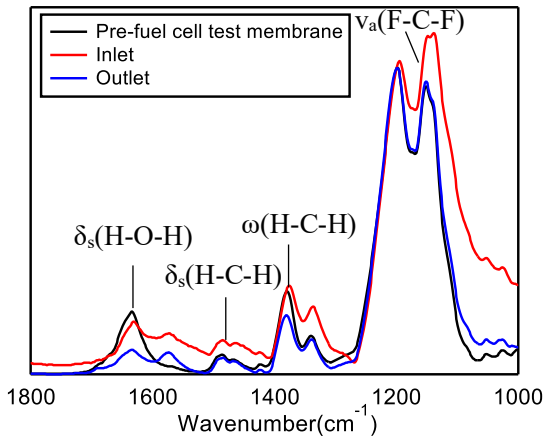

Figure 7: Fourier transform infra-red (FTIR) scan of pre-fuel cell test, post-fuel cell inlet and outlet segment samples. Note: δ_s(H-O-H) - water bending, δ_s(H-C-H)- scissoring of methyl group on quaternary ammonium, ω(H-C-H) - wagging of methyl group on spacer chain and - ν_a(F-C-F) - asymmetric stretching of CF_2 groups in polymer backbone.

The FTIR peaks of this polymer have been characterized in our previous work,(*51*) and are utilized here for the analysis. We noticed that the δ_s(H-O-H) peak at 1650 cm^{-1}, which corresponds to the structure of bound water, has a reduced intensity, and the small peak at 1580 cm^{-1} becomes more pronounced. It is also noticeable that the δ_s(H-C-H) on the quaternary ammonium cation (1465 cm^{-1}) and ω(H-C-H) on the alkyl spacer chain (1380 cm^{-1}) have different intensity for the inlet and the outlet segments. In addition, the scissoring δ_s(H-C-H) peak (1465 cm^{-1}) of the pre-tested membrane sample and the post-tested outlet segment sample overlaps. The data indicate that the quaternary ammonium cation has similar chemical structure before and after fuel cell test for the outlet segment, but not for the inlet segment. Apparently, the degradation is less prevalent near the outlet, which is also supported by the ν_a(F-C-F) peaks (1150 cm^{-1}) that represent the polymer's backbone. The ν_a(F-C-F) peaks for the outlet region also remain unchanged with respect to the pristine materials, while that for the inlet is significantly different in intensity. The change in

backbone peak in the inlet section may also be due to radical attack which was recently reported by Wierzbicki et al [66]. In summary, the data implies that the degradation of the applied AEM polymer is strongly governed by local operating conditions and that degradation rates can vary significantly within the cell.

3.6 Carbonation effect on spatial cell performance:

The presence of CO_2 in the cathode feed stream is highly detrimental to AEM fuel cell performance [1]. This is assigned to the hydroxide charge carrier reacting with the carbon dioxide to form carbonate/bicarbonate ions when ambient air is used as an oxidant [10]. The reaction rapidly affects the ionic conductivity and micro-structure of the membrane [67]. Very recently, it was shown that the ionic conductivity plays a major role in CO_2 related performance loss, whereas polymer crystallinity plays a minor role [68]. Our previously published ex-situ analysis shows that the effect of carbonation is relatively slower at higher hydration levels [10]. Additionally, Mustain and co-workers have shown in-situ comparison of carbonation at different humidity conditions and further optimized the hydration levels in the cell [63]. The reaction is reversible. CO_2 can be purged from the membrane at high current density due to a self-purging phenomenon described in the literature [69]. The following electrochemical/chemical reactions occurring with CO_2 introduction have been suggested [54].

Cathode reactions:

$$O_2 + 2H_2O + 4e^- \rightarrow 4OH^- \quad (1)$$

$$O_2 + 2CO_2 + 4e^- \rightarrow 2CO_3^{2-} \quad (2)$$

$$OH^- + CO_2 \rightarrow HCO_3^- \quad (3)$$

$$HCO3^- + OH^- \rightarrow CO_3^{2-} \quad (4)$$

Anode reactions:

$2H_2 + 4OH^- \rightarrow 4H_2O + 4\ e^-$ (5)

$2H_2 + 2CO_3^{2-} \rightarrow 2H_2O + 2CO_2 + 4e^-$ (6)

$2H_2 + 4HCO_3^- \rightarrow 4H_2O + 4CO_2 + 4e^-$ (7)

These reactions (Equation 1-7) occur simultaneously and they add a significant level of complexity to the AEMFC system. The impact of these complicated reactions and their effects have been studied extensively by Mustain and co-workers [70]. It was previously hypothesized that self-purging by operating the cell at higher current density will ensure that the CO_2 will have minimal effect on cell performance. They conclude that this holds true only when CO_2 in the inlet air stream is below 5 ppm level.

Very recently, Mustain's group as well as Yan's group have introduced a novel concept of utilizing anion exchange CO_2 separation device which can strip 400 ppm CO_2 from the air down to tolerable single digit levels before entering the main AEMFC which is meant to run for longer duration [71, 72]. On the one hand, Yan and co-workers showed that the flow-field design has significant effect on the amount of CO_2 that gets stripped from the air stream. On the other hand, Mustain and co-workers used a 2 stage 25 cm^2 triple pass serpentine flow-field to strip CO_2 concentrations down to below 5 ppm. For the technology to commercialize, both research groups are suggesting that cell engineering is needed to further optimize the design. Therefore, studying the spatial current distribution of a larger cell area exposed to ambient air containing CO_2 becomes very important.

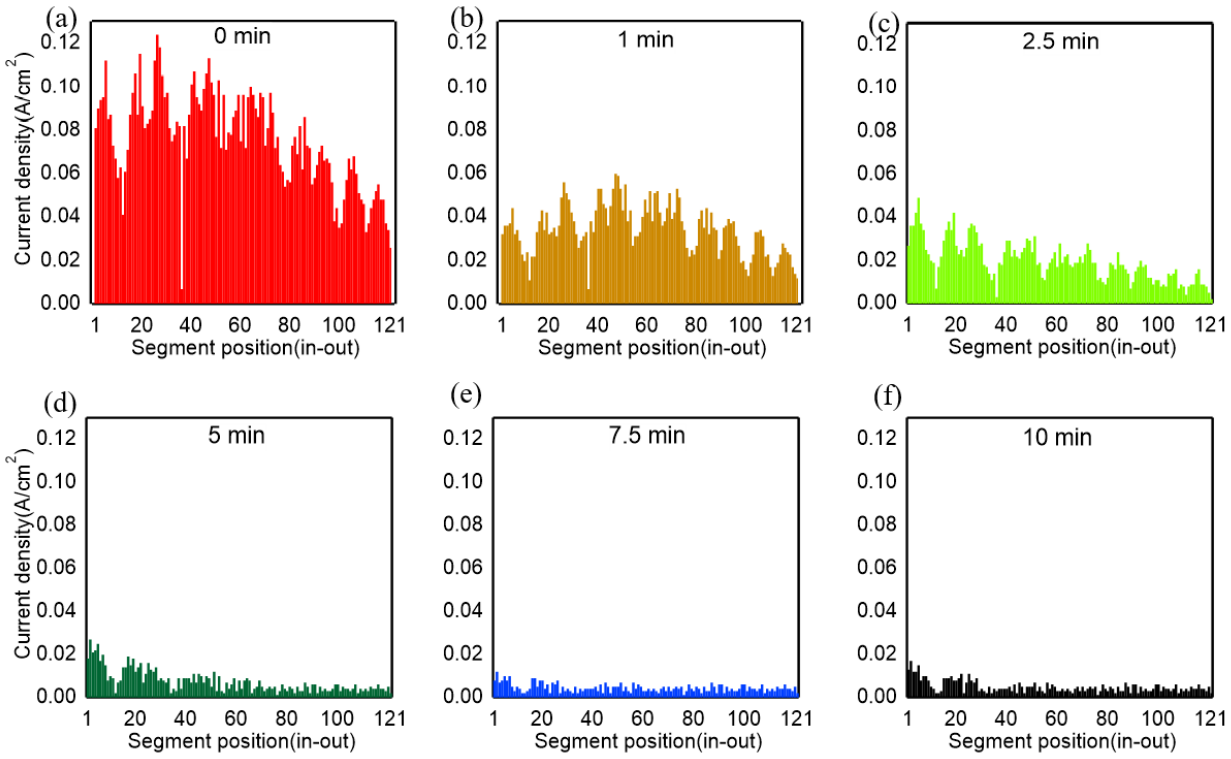

Figure 8: Current distribution over time (a) 0, (b) 1, (c) 2.5, (d) 5, (e) 7.5 & (f) 10 minutes in a serpentine flow-field segmented fuel cell switched to 400ppm CO_2 containing air at a constant voltage of 0.5V at 60 °C, 95/95 %RH at anode/cathode from H_2/Air (<3 ppm CO_2). Note: The flow rates of H_2 and Air (400 ppm CO_2) are 700 sccm and 2600 sccm throughout the experiment of CO_2 containing air exposure.

Figure 8A-F show performance data of each of the 121 segments over the first 10 minutes of operation with air containing 400 ppm CO_2 in the feed stream of the cathode. The cell was initially operated using H_2/Air with less than 3 ppm CO_2 in the feed stream. At time = 0 min, 400 ppm CO_2 was introduced with the air stream into the cell. Subsequently, the performance of the cell rapidly decreased and after about 7.5 minutes the cell could not produce measurable current.

In the absence of CO_2, i.e., t = 0, Figure 8A, the performance fluctuates strongly in the first quarter of the flow-field and then declines towards the outlet. After one minute of CO_2 introduction

(Figure 8B), the overall current density was significantly reduced compared to the $t_0 = 0$ case. The current density still follows the same general trend, i.e. a strong fluctuation over the first third or more of the flow-field followed by a decrease towards the outlet. Beyond 1 min of operation after CO_2 introduction, the spatial current density profile shows a steady decrease of performance along the flow-field and a dramatic loss in the overall cell performance.

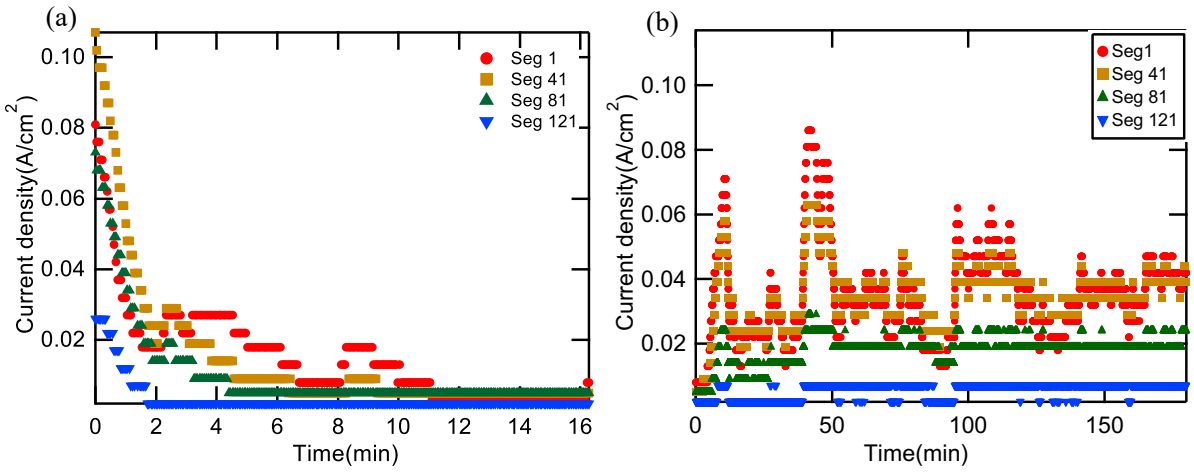

Figure 9: Current density vs time for segment 1, 41, 81 & 121 when the serpentine flow-field segmented cell is (a) exposed to 400 ppm CO_2 containing air from < 3 ppm CO_2 air, (b) exposed to <3 ppm CO_2 air from fully 400 ppm CO_2 containing air equilibrated cell.

Figure 9 shows time resolved data sets for the individual segments 1, 41, 81, and 121 during CO_2 exposure (Figure 9A) and recovery (Figure 9B). While in the first 2 minutes similar degradation rates were initially observed for the entire cell, subsequent segment degradation slowed with respect to the segment position in the cell. As shown in Figure 8C, beyond 2.5 min after CO_2 introduction, the spatial current distribution changed and began to steadily decrease along the flow-field. Before 2.5 min, the inlet segments that are exposed to the incoming CO_2 tend to absorb and self-purge relatively more than the downstream segments. This creates a deficit of CO_2 in the immediate adjacent segments along the flow-channel. This causes an apparent rise in

the performance towards the middle segments, which is not evident after 2.5 mins possibly due to CO_2 saturation in the upstream segments. The data in Figure 9A indicates that with continuing CO_2 exposure the segments closer to the outlet degraded toward zero performance faster than those closer to the inlet. At t_0 the downstream segments 81 and 121 have lower performance than the upstream segments 1 and 41. This suggests that the rate of OH^- production is lower towards the outlet before CO_2 is introduced to the feed stream. With exposure to CO_2, the reaction of OH^- ions with CO_2 at the cathode catalyst layer leads to carbonate formation and transport to the anode. The rate of release of CO_2 from carbonate at the anode is dependent on the current density and occurs faster where the current is highest. However, the CO_2 in the anode also has the ability to reach higher concentrations downstream and also slowing the effective rate of release in downstream segments.

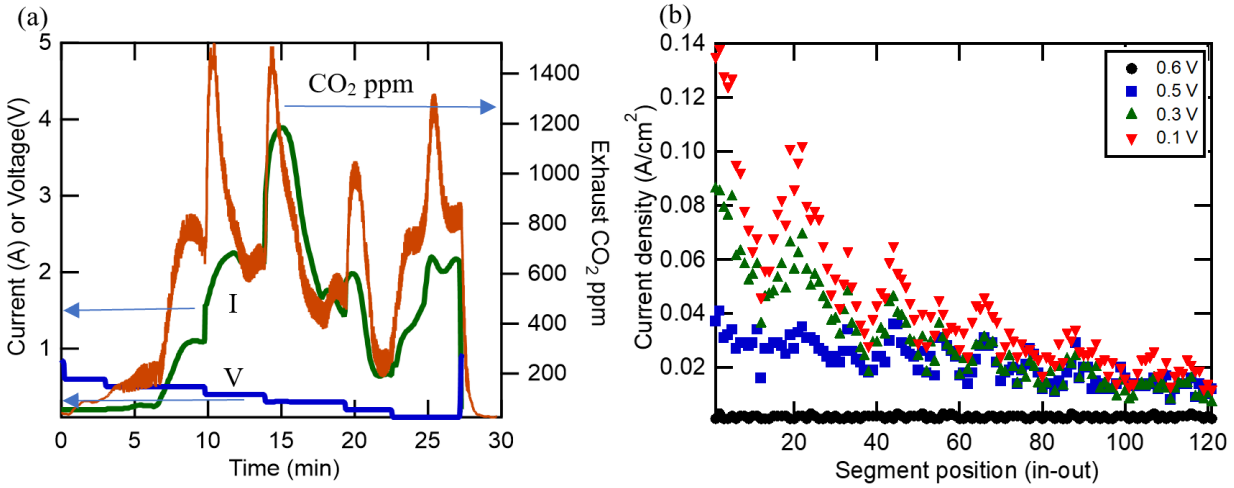

Figure 10: (a) Current, voltage, and CO_2 anode exhaust ppm vs time of a fully air equilibrated cell at 60 °C, 95/95% RH at anode/cathode from H_2/ Air (400 ppm CO_2). (b) Spatial current profile of cell held at 0.6 (black circles), 0.5 (blue squares), 0.3 (green triangles), and 0.1 (red inverted triangles) V.

After the cell was equilibrated in 400 ppm CO_2, the cell was held at different voltages to study

the spatial current distribution as well as the CO_2 which gets purged from the anode was monitored in the exhaust stream. The data of voltage, CO_2 exhaust ppm, current density vs time is shown in figure 10A. The data shows that the overall performance of the cell is negligible > 0.5V, below 0.5 V, the cell performance increases and simultaneously CO_2 is observed to be purged from the anode exhaust. For voltage < 0.3, the performance suffers due to excessive flooding in the downstream segments which is evident from spatial current data in figure 10B. Interestingly, the CO_2 ppm in the exhaust also reduces at lower voltages. The spatial current data in figure 10B indicate that the cell performance is disproportionately higher in the inlet segment due to flooding in the downstream segments. This may cause unequal degradation over prolonged operation of the cell as shown in figure 6. Therefore, it is recommended to operate the cell at lower current density to avoid flooding and also to optimize the amount of CO_2 purged through the anode for the application of anion exchange membrane CO_2 separation device.

Later, the performance recovery of the cell was induced by switching the oxidant feedback to < 3 ppm CO_2 air with the intention to decarbonate the cell. Figure 9B shows recovery data of the previously discussed 4 segments over time, and Figure 11 shows current density distribution snap shots over a period of 13 h. The data indicate that the decarbonation leads to a decreasing current distribution profile along the flow-field, likely due to upstream segments decarbonating first. Even after 13 h of cell recovery in < 3 ppm CO_2 air (Figure 11F), the cell did not completely retrieve its original performance (Figure 8A). One effective recovery strategy is to operate the cell with a pure O_2 feed stream over a period of time. As discussed above, another recovery strategy is to release CO_2 through a self-purging process, i.e., operation in pure air without CO_2. We have discussed in previous work that this process is more effective at lower voltages. The results of that study further suggest that the ionic conductivity of a carbonated sample is almost completely recovered after

48 h of exposure to CO_2 free conditions [10].

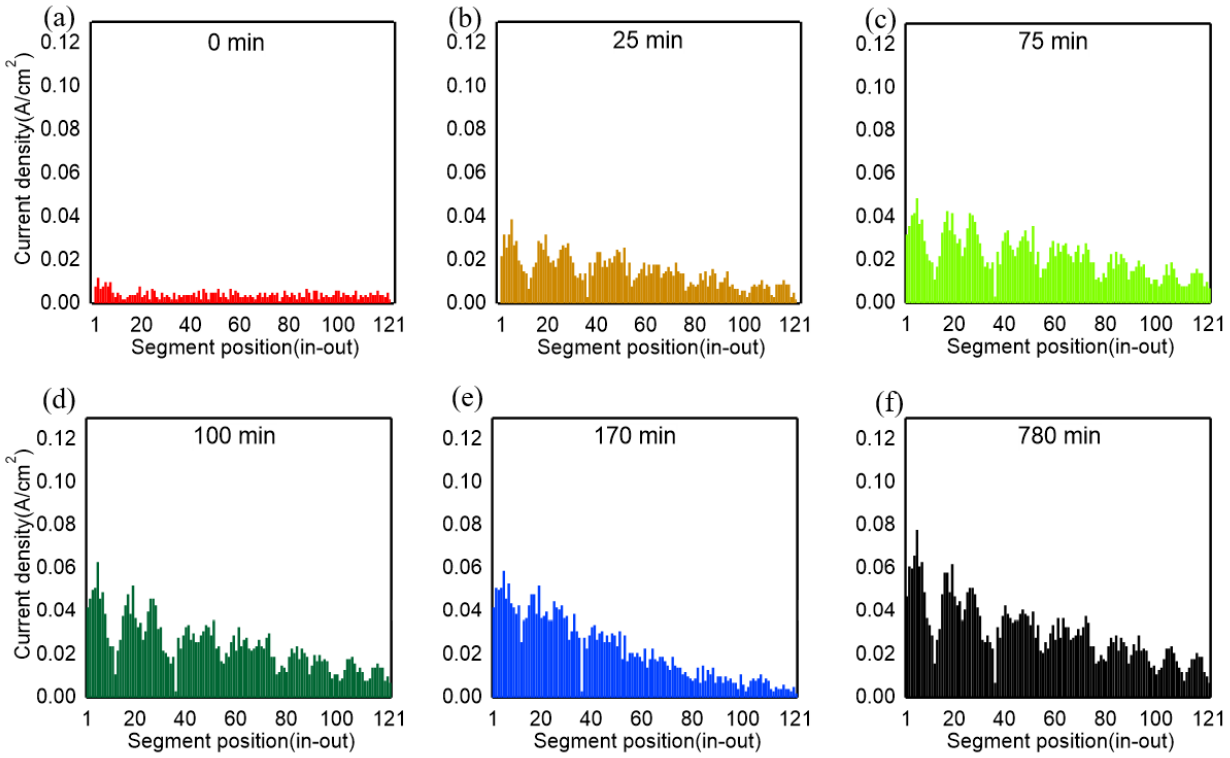

Figure 11: Current distribution over time (a) 0, (b) 25, (c) 75, (d) 100, (e) 170 & (f) 780 minutes in a serpentine flow-field segmented fuel cell switched to <3 ppm CO_2 containing air at a constant voltage of 0.5V at 60 °C, 95/95 %RH at anode/cathode from H_2/Air (400 ppm CO_2) at time 0 min. Note: The flow rates of H_2 and Air (<3 ppm CO_2) are 700 and 2600 sccm respectively.

The overpotential losses due to CO_2 inclusion are primarily due to kinetic deactivation of the anode catalyst layer [56]. High current density, low cell potential operation has been shown to be important for purging of the carbon-dioxide from the AEMFC system [9, 73]. However, Zheng et al. has shown that CO_2 concentrations as low as 5 ppm can be detrimental to the cell performance and also self-purging by itself cannot be relied to decarbonate the cell completely [70]. However, optimizing the cell operating conditions and designing better flow-fields will enable this technology to be used as a sacrificial fuel cell to separate CO_2 from the air stream prior to feeding

it to the main fuel cell for power generation.

4. Conclusions:

A SFC hardware was used to shed light on two high-level phenomena: 1. The effect of key operating conditions such as hydration, flow rate, and concentration, and 2. the loss in cell performance due to OH^- attack and carbonation observed in a perfluorinated anion exchange membrane fuel cell. The fuel cell was tested using two kinds of flow-field architectures: serpentine and straight channel. The straight channel cell study eliminates the non-uniformity of current distribution observed in the edge segments and in-plane shortcut flows through the GDL.

From hydration experiments, the decline in the cell performance occurs due to anode flooding or cathode drying. The latter is the more severe case because the cathode experiences a deficit in the water supply due to its consumption of water in the oxygen reduction reaction and the electro-osmotic drag of H_2O molecules from the cathode to the anode compartment. Modeling results suggest that the non-uniformities in current distribution observed in the serpentine case can be attributed to periodic changes in mass transport due to the flow-field structure. Any anode drying doesn't affect the performance as much because H_2O molecules are produced at the anode and additionally the electro-osmotic drag transports them from the cathode to the anode compartment.

The reduction in the flow rate of inlet gas affects the cell performance minimally for both anode as well as the cathode compartment. The discrepancy in the cell performance is visible when the feed gas is diluted with the N_2 stream which mainly affects the mass-transfer (high current density operation) region of anode/cathode dilution experiments. Limiting current density is observed at lower dilutions of 25 and 5% H_2/O_2 but the cell performance is more sensitive to anode dilution. The spatial current density profile indicates that the cell performance distribution gets severely affected at the inlet segments (first four segments) due to anode feed dilution whereas a

uniform decrease is observed throughout the flow-channel due to cathode feed dilution.

The cell degrades over the time of 26 days with significant performance losses in the inlet section and a minimal loss in the outlet section which suggests that the cell degradation is slower in the downstream segments possibly due to lower current densities and better hydration which limit chemical degradation. FTIR analysis before and after the fuel cell test shows a difference in the intensity of chemical peaks with respect to segment position. This confirms that there is a change in the bound water, quaternary ammonium on the side chain, and the polymer backbone near the outlet segments due to the difference in the δ_s(H-O-H) bend, δ_s(H-C-H) scissoring, ω(H-C-H) wagging and the ν_a(F-C-F) asymmetric stretch. Furthermore, modeling results also show higher dryout on the cathode due to high current operation at the inlet segments. This gets more pronounced due to reduced water transport over prolonged operation and hence contribute to observed degradation near the cell inlet.

On introduction of CO_2, the carbonation of the OH^- charge carrier in the AEM leads to a loss in cell performance within 7.5 minutes. The inlet segments take a longer time to show performance loss compared to outlet segments. After air equilibration, the voltage hold indicates that the cell performance suffers below 0.3V, which causes lowering of the CO_2 purge in the anode exhaust and also may cause disproportionate degradation over prolonged operation in the active area. The performance recovery due to decarbonation process occurs at a uniform but slower rate throughout the cell. However, the performance never completely recovered to pre-CO_2 exposure levels for the conditions tested which was attributed to insufficient current density to decarbonate the cell.

Much future work remains to be done such as the investigation of co- and counter flow configuration, effect of temperature gradients, water balances, ex-situ SEM/TEM diagnostics, or changes in ECSA and expanding the work to AEM electrolyzers [74,75]. Water slugs could also

exist in the flow fields at higher humidification and lower flow rates resulting in transient spikes in performance, that should be a focus of future study.

Acknowledgments

The work was supported by the U.S. Department of Energy under Contract No. DE-AC36-08GO28308 with Alliance for Sustainable Energy, LLC, the Manager and Operator of the National Renewable Energy Laboratory. Funding provided by the U.S. Department of Energy Office of Energy Efficiency and Renewable Energy Fuel Cell Technologies Office. The views and opinions of the authors expressed herein do not necessarily state or reflect those of the United States Government or any agency thereof. Neither the United States Government nor any agency thereof, or any of their employees, makes any warranty, expressed or implied, or assumes any legal liability or responsibility for the accuracy, completeness, or usefulness of any information, apparatus, product, or process disclosed, or represents that its use would not infringe privately owned rights. The U.S. Government retains and the publisher, by accepting the article for publication, acknowledges that the U.S. Government retains a nonexclusive, paid-up, irrevocable, worldwide license to publish or reproduce the published form of this work, or allow others to do so, for U.S. Government purposes.

References:

1. J. R. Varcoe *et al.*, Anion-exchange membranes in electrochemical energy systems. *Energy & Environmental Science* 7 (2014) 3135-3191.
2. A. Kongkanand, M. F. Mathias, The Priority and Challenge of High-Power Performance of Low-Platinum Proton-Exchange Membrane Fuel Cells. *The Journal of Physical Chemistry Letters* 7 (2016) 1127-1137.
3. G. Merle, M. Wessling, K. Nijmeijer, Anion exchange membranes for alkaline fuel cells: A review. *Journal of Membrane Science* 377 (2011) 1.
4. D. R. Dekel, Review of cell performance in anion exchange membrane fuel cells. *Journal of Power Sources* 375 (2018) 158-169.
5. A. G. Divekar, B. S. Pivovar, A. M. Herring, Kinetic Equilibrium Study of CO2 Poisoning Observed in Anion Exchange Membranes When Exposed to Ambient Air and Varying Levels of CO2 ppm. *ECS Transactions* 86 (2018) 643-648.

6. W. E. Mustain, M. Chatenet, M. Page, Y. S. Kim, Durability challenges of anion exchange membrane fuel cells. *Energy & Environmental Science* 13 (2020) 2805-2838.
7. N. Ul Hassan *et al.*, Achieving High-Performance and 2000 h Stability in Anion Exchange Membrane Fuel Cells by Manipulating Ionomer Properties and Electrode Optimization. *Advanced Energy Materials* 10 (2020) 2001986.
8. M. G. Marino, K. D. Kreuer, Alkaline Stability of Quaternary Ammonium Cations for Alkaline Fuel Cell Membranes and Ionic Liquids. *ChemSusChem* 8 (2015) 513-523.
9. N. Ziv, A. N. Mondal, T. Weissbach, S. Holdcroft, D. R. Dekel, Effect of CO2 on the properties of anion exchange membranes for fuel cell applications. *Journal of Membrane Science* 586 (2019) 140-150.
10. A. G. Divekar *et al.*, In-depth understanding of the CO2 limitation of air fed anion exchange membrane fuel cells. *Sustainable Energy & Fuels* 4 (2020) 1801-1811.
11. N. C. Buggy *et al.*, A Polyethylene-Based Triblock Copolymer Anion Exchange Membrane with High Conductivity and Practical Mechanical Properties. *ACS Applied Polymer Materials* 2 (2020) 1294-1303.
12. M. Mandal, G. Huang, P. A. Kohl, Highly Conductive Anion-Exchange Membranes Based on Cross-Linked Poly(norbornene): Vinyl Addition Polymerization. *ACS Applied Energy Materials* 2 (2019) 2447-2457.
13. W. Zhang *et al.*, Crosslinked anion exchange membranes with connected cations. *Journal of Polymer Science Part A: Polymer Chemistry* 56 (2018) 618-625.
14. G. Huang *et al.*, Composite Poly(norbornene) Anion Conducting Membranes for Achieving Durability, Water Management and High Power (3.4 W/cm2) in Hydrogen/Oxygen Alkaline Fuel Cells. *Journal of The Electrochemical Society* 166 (2019) F637-F644.
15. A. M. Herring *et al.*, (Invited) The Implications of Cation Clustering in Anion Exchange Membranes on Conductivity and Mechanical Properties. *ECS Transactions* 75 (2016) 945-948.
16. J. Wang *et al.*, Structure–Property Relationships in Hydroxide-Exchange Membranes with Cation Strings and High Ion-Exchange Capacity. *ChemSusChem* 8 (2015) 4229-4234.
17. H. Herman, R. C. T. Slade, J. R. Varcoe, The radiation-grafting of vinylbenzyl chloride onto poly(hexafluoropropylene-co-tetrafluoroethylene) films with subsequent conversion to alkaline anion-exchange membranes: optimisation of the experimental conditions and characterisation. *Journal of Membrane Science* 218 (2003) 147-163.
18. J. R. Varcoe *et al.*, Poly(ethylene-co-tetrafluoroethylene)-Derived Radiation-Grafted Anion-Exchange Membrane with Properties Specifically Tailored for Application in Metal-Cation-Free Alkaline Polymer Electrolyte Fuel Cells. *Chemistry of Materials* 19 (2007) 2686-2693.
19. J. R. Varcoe, R. C. T. Slade, An electron-beam-grafted ETFE alkaline anion-exchange membrane in metal-cation-free solid-state alkaline fuel cells. *Electrochemistry Communications* 8 (2006) 839-843.
20. O. I. Deavin *et al.*, Anion-exchange membranes for alkaline polymer electrolyte fuel cells: comparison of pendent benzyltrimethylammonium- and benzylmethylimidazolium-head-groups. *Energy & Environmental Science* 5 (2012) 8584-8597.
21. J. Ponce-Gonzlez *et al.*, High performance aliphatic-heterocyclic benzyl-quaternary ammonium radiation-grafted anion-exchange membranes. *Energy & Environmental Science* 9 (2016) 3724-3735.

22. A. G. Divekar *et al.*, Thin Film Morphological Characteristics of a Perfluorinated Anion Exchange Membrane. *ECS Transactions* 92 (2019) 715-722.
23. S. J. C. Cleghorn, C. R. Derouin, M. S. Wilson, S. Gottesfeld, A printed circuit board approach to measuring current distribution in a fuel cell. *Journal of Applied Electrochemistry* 28 (1998) 663-672.
24. J. Stumper, S. A. Campbell, D. P. Wilkinson, M. C. Johnson, M. Davis, In-situ methods for the determination of current distributions in PEM fuel cells. *Electrochimica Acta* 43 (1998) 3773-3783.
25. G. Bender, M. S. Wilson, T. A. Zawodzinski, Further refinements in the segmented cell approach to diagnosing performance in polymer electrolyte fuel cells. *Journal of Power Sources* 123 (2003) 163-171.
26. C. Wieser, A. Helmbold, E. Gülzow, A new technique for two-dimensional current distribution measurements in electrochemical cells. *Journal of Applied Electrochemistry* 30 (2000) 803-807.
27. D. J. L. Brett *et al.*, Measurement of the current distribution along a single flow channel of a solid polymer fuel cell. *Electrochemistry Communications* 3 (2001) 628-632.
28. L. C. Pérez, L. Brandão, J. M. Sousa, A. Mendes, Segmented polymer electrolyte membrane fuel cells—A review. *Renewable and Sustainable Energy Reviews* 15 (2011) 169-185.
29. S. Cleghorn, C. Derouin, M. Wilson, S. Gottesfeld, A printed circuit board approach to measuring current distribution in a fuel cell. *Journal of Applied Electrochemistry* 28 (1998) 663-672.
30. M. Noponen, J. Ihonen, A. Lundblad, G. Lindbergh, Current distribution measurements in a PEFC with net flow geometry. *Journal of Applied Electrochemistry* 34 (2004) 255-262.
31. S. Yoshioka, A. Yoshimura, H. Fukumoto, O. Hiroi, H. Yoshiyasu, Development of a PEFC under low humidified conditions. *Journal of Power Sources* 144 (2005) 146-151.
32. F.-B. Weng, B.-S. Jou, C.-W. Li, A. Su, S.-H. Chan, The effect of low humidity on the uniformity and stability of segmented PEM fuel cells. *Journal of Power Sources* 181 (2008) 251-258.
33. T. Hottinen *et al.*, Effect of ambient conditions on performance and current distribution of a polymer electrolyte membrane fuel cell. *Journal of Applied Electrochemistry* 33 (2003) 265-271.
34. Y. Tabe, K. Kikuta, T. Chikahisa, M. Kozakai, Basic evaluation of separator type specific phenomena of polymer electrolyte membrane fuel cell by the measurement of water condensation characteristics and current density distribution. *Journal of Power Sources* 193 (2009) 416-424.
35. A. Hakenjos, H. Muenter, U. Wittstadt, C. Hebling, A PEM fuel cell for combined measurement of current and temperature distribution, and flow field flooding. *Journal of Power Sources* 131 (2004) 213-216.
36. X.-G. Yang, N. Burke, C.-Y. Wang, K. Tajiri, K. Shinohara, Simultaneous Measurements of Species and Current Distributions in a PEFC under Low-Humidity Operation. *Journal of The Electrochemical Society* 152 (2005) A759-A766.
37. Q. Dong, M. M. Mench, S. Cleghorn, U. Beuscher, Distributed Performance of Polymer Electrolyte Fuel Cells under Low-Humidity Conditions. *Journal of The Electrochemical Society* 152 (2005) A2114-A2122.
38. Y. Morimoto, T. Suzuki, H. Yamada, Measurement of the Distributions of Local Current

Density and Local Ionic Resistance of PEFCs. *ECS Proceedings Volumes* 31 (2002) 248-256.
39. M. Hicks, K. Kropp, A. Schmoeckel, R. Atanasoski, Current Distribution along a Quad-Serpentine Flow Field: GDL Evaluation. *ECS Transactions* 1 (2006) 605-612.
40. G. Maranzana, O. Lottin, T. Colinart, S. Chupin, S. Didierjean, A multi-instrumented polymer exchange membrane fuel cell: Observation of the in-plane non-homogeneities. *Journal of Power Sources* 180 (2008) 748-754.
41. A. A. Kulikovsky, A. Kucernak, A. A. Kornyshev, Feeding PEM fuel cells. *Electrochimica Acta* 50 (2005) 1323-1333.
42. P. C. Ghosh *et al.*, In situ approach for current distribution measurement in fuel cells. *Journal of Power Sources* 154 (2006) 184-191.
43. F. N. Büchi, A. B. Geiger, R. P. Neto, Dependence of current distribution on water management in PEFC of technical size. *Journal of Power Sources* 145 (2005) 62-67.
44. Z. Liu, Z. Mao, B. Wu, L. Wang, V. M. Schmidt, Current density distribution in PEFC. *Journal of Power Sources* 141 (2005) 205-210.
45. J. Stumper, M. Löhr, S. Hamada, Diagnostic tools for liquid water in PEM fuel cells. *Journal of Power Sources* 143 (2005) 150-157.
46. J. J. Hwnag, W. R. Chang, R. G. Peng, P. Y. Chen, A. Su, Experimental and numerical studies of local current mapping on a PEM fuel cell. *International Journal of Hydrogen Energy* 33 (2008) 5718-5727.
47. T. Tingelöf, L. Hedström, N. Holmström, P. Alvfors, G. Lindbergh, The influence of CO2, CO and air bleed on the current distribution of a polymer electrolyte fuel cell. *International Journal of Hydrogen Energy* 33 (2008) 2064-2072.
48. T. V. Reshetenko, K. Bethune, R. Rocheleau, Spatial proton exchange membrane fuel cell performance under carbon monoxide poisoning at a low concentration using a segmented cell system. *Journal of Power Sources* 218 (2012) 412-423.
49. D. J. L. Brett, P. Aguiar, N. P. Brandon, A. R. Kucernak, Measurement and modelling of carbon monoxide poisoning distribution within a polymer electrolyte fuel cell. *International Journal of Hydrogen Energy* 32 (2007) 863-871.
50. A. M. Park *et al.*, Synthesis and Characterization of Perfluorinated Anion Exchange Membranes. *ECS Transactions* 80 (2017) 957-966.
51. A. G. Divekar *et al.*, The impact of alkyl tri-methyl ammonium side chains on perfluorinated ionic membranes for electrochemical applications. *Journal of Polymer Science Part B: Polymer Physics* 57 (2019) 700-712.
52. A. Phillips, M. Ulsh, J. Porter, G. Bender, Utilizing a Segmented Fuel Cell to Study the Effects of Electrode Coating Irregularities on PEM Fuel Cell Initial Performance. *Fuel Cells* 17 (2017) 288-298.
53. T. J. Omasta *et al.*, Beyond catalysis and membranes: visualizing and solving the challenge of electrode water accumulation and flooding in AEMFCs. *Energy & Environmental Science* 11 (2018) 551-558.
54. N. Ziv, W. E. Mustain, D. R. Dekel, The Effect of Ambient Carbon Dioxide on Anion-Exchange Membrane Fuel Cells. *ChemSusChem* 11 (2018) 1136-1150.
55. L. Osmieri, S. Mauger, M. Ulsh, K. C. Neyerlin, G. Bender, Use of a segmented cell for the combinatorial development of platinum group metal-free electrodes for polymer electrolyte fuel cells. *Journal of Power Sources* 452 (2020) 227829.
56. M. R. Gerhardt, L. M. Pant, A. Z. Weber, Along-the-Channel Impacts of Water

Management and Carbon-Dioxide Contamination in Hydroxide-Exchange-Membrane Fuel Cells: A Modeling Study. *Journal of The Electrochemical Society* 166 (2019) F3180-F3192.
57. A. Z. Weber, J. Newman, Transport in Polymer-Electrolyte Membranes II. Mathematical Model. *Journal of The Electrochemical Society* 151 (2004) A311.
58. H.-S. Shiau, I. V. Zenyuk, A. Z. Weber, Elucidating Performance Limitations in Alkaline-Exchange- Membrane Fuel Cells. *Journal of The Electrochemical Society* 164 (2017) E3583-E3591.
59. J. Zhou, A. Putz, M. Secanell, A Mixed Wettability Pore Size Distribution Based Mathematical Model for Analyzing Two-Phase Flow in Porous Electrodes. *Journal of The Electrochemical Society* 164 (2017) F530-F539.
60. X. Peng *et al.*, Using operando techniques to understand and design high performance and stable alkaline membrane fuel cells. *Nature Communications* 11 (2020) 3561.
61. T. Mennola, M. Noponen, T. Kallio, M. Mikkola, T. Hottinen, Water balance in a free-breathing polymer electrolyte membrane fuel cell. *Journal of Applied Electrochemistry* 34 (2004) 31-36.
62. T. J. Omasta *et al.*, Importance of balancing membrane and electrode water in anion exchange membrane fuel cells. *Journal of Power Sources* 375 (2018) 205-213.
63. Y. Zheng *et al.*, Effect of reacting gas flowrates and hydration on the carbonation of anion exchange membrane fuel cells in the presence of CO2. *Journal of Power Sources* 467 (2020) 228350.
64. C. Lafforgue, F. Maillard, V. Martin, L. Dubau, M. Chatenet, Degradation of Carbon-Supported Platinum-Group-Metal Electrocatalysts in Alkaline Media Studied by in Situ Fourier Transform Infrared Spectroscopy and Identical-Location Transmission Electron Microscopy. *ACS Catalysis* 9 (2019) 5613-5622.
65. J. Müller, A. Zhegur, U. Krewer, J. R. Varcoe, D. R. Dekel, Practical ex-Situ Technique To Measure the Chemical Stability of Anion-Exchange Membranes under Conditions Simulating the Fuel Cell Environment. *ACS Mater Lett* 2 (2020) 168-173.
66. S. Wierzbicki, J. C. Douglin, A. Kostuch, D. R. Dekel, K. Kruczała, Are Radicals Formed During Anion-Exchange Membrane Fuel Cell Operation? *The Journal of Physical Chemistry Letters* 11 (2020) 7630-7636.
67. A. G. Divekar *et al.*, A Study of Carbonate Formation Kinetics and Morphological Effects Observed on OH- Form of Pfaem When Exposed to Air Containing CO2. *ECS Transactions* 80 (2017) 1005-1011.
68. Y. Zheng *et al.*, Effect of Membrane Properties on the Carbonation of Anion Exchange Membrane Fuel Cells. *Membranes* 11 (2021) 102.
69. S. Suzuki, H. Muroyama, T. Matsui, K. Eguchi, Influence of CO2dissolution into anion exchange membrane on fuel cell performance. *Electrochimica Acta* 88 (2013) 552-558.
70. Y. Zheng *et al.*, Quantifying and elucidating the effect of CO 2 on the thermodynamics, kinetics and charge transport of AEMFCs. *Energy & Environmental Science* 12 (2019) 2806-2819.
71. Y. Zheng *et al.*, Editors' Choice—Power-Generating Electrochemical CO2 Scrubbing from Air Enabling Practical AEMFC Application. *Journal of the Electrochemical Society* 168 (2021) 024504.
72. S. Matz *et al.*, Demonstration of Electrochemically-Driven CO2 Separation Using Hydroxide Exchange Membranes. *Journal of The Electrochemical Society* 168 (2021)

014501.
73. K. Fukuta, H. Inoue, S. Watanabe, H. Yanagi, In-situ Observation of CO2 through the Self-purging in Alkaline Membrane Fuel Cell (AMFC). *ECS Transactions* 19 (2009) 23-27.
74. A. C. Yang-Neyerlin *et al.*, Editors' Choice—Examining Performance and Durability of Anion Exchange Membrane Fuel Cells with Novel Spirocyclic Anion Exchange Membranes. *Journal of The Electrochemical Society* 168 (2021) 044525.
75. I. Biswas *et al.*, Advancement of Segmented Cell Technology in Low Temperature Hydrogen Technologies. *Energies* 13 (2020) 2301.